Did Late Miocene (Messinian) gypsum precipitate from evaporated marine brines? Insights from the Piedmont Basin (Italy)

(Article begins on next page)

07 January 2023

1   # Did the Late Miocene (Messinian) gypsum precipitate from

2   # evaporated marine brines? Insights from the Piedmont Basin

3   # (Italy)

4   **Marcello Natalicchio[1]***, **Francesco Dela Pierre[1], Stefano Lugli[2], Tim K. Lowenstein[3],**

5   **Sarah J. Feiner[3], Simona Ferrando[1], Vinicio Manzi[4], Marco Roveri[4], and Pierangelo**

6   **Clari[1]**

7   [1]*Dipartimento di Scienze della Terra, Università di Torino, 10125 Torino, Italy*

8   [2]*Dipartimento di Scienze Chimiche e Geologiche, Università di Modena e Reggio Emilia,*

9   *41100 Modena, Italy*

10   [3]*Department of Geological Sciences & Environmental Studies, State University of New York,*

11   *Binghamton, 13902 New York, USA*

12   [4]*Dipartimento di Fisica e Scienze della Terra, Università di Parma, 43100 Parma, Italy*

13   *E-mail: marcello.natalicchio@unito.it.

14   **ABSTRACT**

15   During the first stage of the Late Miocene Messinian salinity crisis (5.97 - 5.60 Ma)

16   deposition of sulfates (Primary Lower Gypsum) occurred in shallow silled peripheral sub-

17   basins of the Mediterranean experiencing restricted water exchange with the Atlantic Ocean.

18   Fluid inclusions in Messinian selenite crystals from the Piedmont Basin (NW Italy) have

19   surprisingly low salinities (average of 1.6 weight % NaCl equivalent), suggesting parent

20   waters depleted in Na^+ and Cl^- compared to modern seawater. Modern gypsum from a

21   Mediterranean saltwork, in contrast, contains fluid inclusions with elevated salinities that

22   match the normal evaporation trend expected for seawater. The salinity data indicate that the

23   Messinian sulfate deposits from the Piedmont Basin formed from hybrid parent waters:

24   seawater mixed with Ca^{2+} and SO_4^{2-} enriched freshwaters that dissolved coeval marginal

25 marine gypsum. Such mixed parent waters and complex recycling processes should be taken

26 into account when explaining the genesis of other Messinian gypsum deposits across the

27 Mediterranean Basin.

28 **INTRODUCTION**

29 Since the 1970s, numerous studies have reconstructed the depositional paleoenvironments of

30 Late Miocene sulfates and the paleohydrology of the Mediterranean during the Messinian

31 salinity crisis (CIESM, 2008). However, estimates of the composition and salinity of brines

32 from which large volumes of sulfates formed are still scarce and have been mostly obtained

33 by isotope geochemistry (e.g., Pierre and Fontes, 1978; Longinelli, 1979). Chemical analyses

34 of fluid inclusions in saline minerals are a powerful tool for the estimation of brine

35 composition (Lowenstein et al., 2001, 2003; Horita et al., 2002; Brennan et al., 2004). A

36 second technique, fluid inclusion microthermometry, is grounded on the fact that dissolved

37 salts depress the freezing (and melting) temperature of water (ice). Few studies have used this

38 technique on fluid inclusion in modern and ancient gypsum to determine brine salinities (e.g.,

39 Sabouraud-Rosset, 1976; Attia et al., 1995).

40 Here we present results from fluid inclusions in gypsum from the Messinian Primary

41 Lower Gypsum unit (Roveri et al., 2008) of the Piedmont Basin (NW Italy) and from modern

42 gypsum from the Conti Vecchi solar saltworks (Sardinia, Italy). We compare the melting

43 behavior of fluid inclusions in modern marine gypsum, for which the composition and

44 salinity of the parent brines are known, with that of the inclusions trapped in Messinian

45 gypsum, for which the parent water chemistry is unknown. This comparative study reveals

46 that Messinian gypsum did not form from the normal evaporation of seawater.

47 **THE MESSINIAN PRIMARY LOWER GYPSUM**

48 The Primary Lower Gypsum (PLG; CIESM, 2008; Roveri et al., 2008) formed during

49 the first stage of the Messininan salinity crisis (5.97–5.60 Ma; Manzi et al., 2013) in silled

50 peripheral basins of the Mediterranean area (Lugli et al., 2010; Fig. 1A). The marked

51 lithologic cyclicity of these deposits, defined by decametric-scale gypsum-mud couplets, is

52 ascribed to precession-driven dry-wet climate oscillations (Krijgsman et al., 1999).

53   We analyzed gypsum samples collected in two sections of the Piedmont Basin

54 (Banengo and Moncucco; Dela Pierre et al., 2007; 2011; Natalicchio et al., 2013; Fig. 1B)

55 showing the lowermost four PLG cycles made up of 15–30 m-thick gypsum beds,

56 interbedded with 1–2 m-thick mudstone layers (Fig. 2A). The lowermost three gypsum beds

57 consist of massive selenite with meter to centimeter-sized twinned crystals (Fig. 2B); the

58 fourth bed is made up of banded selenite, composed of centimeter and millimeter thick

59 crystal crusts separated by clay laminae. The textures and thicknesses of the sampled gypsum

60 beds are remarkably similar to the PLG deposits of the other Mediterranean basins (Lugli et

61 al., 2010; Fig. 1A). In particular, alternations of millimeter to centimeter thick turbid and

62 limpid intervals are observed in the re-entrant angle of the twinned crystals (Fig. 2B). The

63 turbid intervals contain clay-rich aggregates, marine (e.g., *Trigonium* sp.) and brackish (e.g.,

64 *Surirella* sp.) water diatoms (Bonci, personal commun.), and curved filaments ("spaghetti-

65 like structures"; Panieri et al., 2010). Limpid intervals are mostly devoid of solid inclusions.

66 **THE MODERN GYPSUM**

67   Modern gypsum was sampled at the Conti Vecchi solar saltworks, Sardinia, a

68 complex of ~50 gypsum and halite crystallizer ponds through which Mediterranean seawater

69 is pumped in order to concentrate brine by evaporation. Gypsum crystals, up to 9 cm tall,

70 with elongate asymmetric habits and curved faces, were sampled in spring 2012 from

71 decimeter-sized domes (Fig. 2C) growing on the bottom of shallow ponds, less than 1 m in

72 depth. The chemical composition of a typical gypsum pond brine is shown in Table 1.

73 **MICROTHERMOMETRIC ANALYSIS**

74   Seven samples from the Messinian sections and three samples from the modern

75   saltworks were used for microthermometry (Attia et al., 1995; see details of methodology in

76   GSA Data Repository).

77   Three types of aqueous inclusions are trapped within Messinian gypsum. The first

78   type is marked by three- to six-sided geometrical shapes (Figs. 2D, E); groups of inclusions,

79   10–130 μm in size, are present within the re-entrant angle of the crystals and are aligned

80   parallel to crystal growth surfaces. These are considered primary inclusions and were used for

81   microthermometric studies. All these inclusions consist of a single-phase liquid, which, after

82   stretching by freezing, (see methods in the GSA Data Repository), became two-phase (liquid

83   + vapor) (Fig. 2E). The second type consists of prismatic to rounded elongated inclusions, up

84   to 100 μm long; they are arranged along the 010 cleavage plane, with the major axis parallel

85   to the 100 plane (Fig. 2F), and are thus interpreted as secondary (e.g., Attia et al., 1995). The

86   third type consists of micron-sized inclusions aligned along fractures, thus secondary or

87   pseudo-secondary in origin.

88   Primary inclusions in Messinian gypsum froze at −40 °C to −60 °C, with

89   simultaneous shrinkage of the vapor bubble. During heating, first melting was observed

90   between −38 °C and −35 °C (Table DR1). With further heating two solid phases were

91   observed: one, more abundant, had low relief and a rounded habit (probably ice); the other

92   had high relief (probably hydrohalite, $NaCl \cdot 2H_2O$). The putative hydrohalite completely

93   melted between −23 °C and −19 °C (Tm_{Hhl}) and at higher temperatures only rounded ice

94   crystals remained within inclusions (Fig. 2E). The final melting temperature of ice (Tm_{ice}) for

95   90 fluid inclusions was between −4.9 °C and −0.1 °C with the majority between −1.5 °C and

96   −0.1 °C (Fig. DR1).

97   In the Conti Vecchi gypsum, primary inclusions, up to 200 μm in size, show

98   elongated and triangular shapes (Fig. 2G). Secondary micron-sized inclusions, mainly aligned

99   along fractures, are also present. Three types of primary inclusions are observed: 1) single

100   phase (aqueous); 2) two phase (aqueous + vapor); 3) three phase (aqueous + vapor + halite);

101   only 1 and 2 phase inclusions were selected for microthermometry. They froze at

102   temperatures below −55 °C. During heating, a first re-organization occurred between −55 °C

103   and −45 °C corresponding to the first melting of Mg-chloride hydrate, the main ultra low

104   temperature hydrated salt in frozen seawater (Davis et al., 1990). Between −30 °C and −21

105   °C, two solid phases with different relief and habit were distinguished. One solid melted

106   completely at ~−21 °C (±0.2 °C), close to the $NaCl$-H_2O eutectic point. This melted solid is

107   clearly ice, and not hydrohalite, because of its low relief. Moreover the remaining un-melted

108   solid phase (Fig. 2H), when re-cooled, exhibited the hexagonal habit diagnostic of

109   hydrohalite (Davis et al., 1990). The final melting temperature of hydrohalite was between

110   −0.5 °C and 0 °C (±0.2 °C).

111   **MODERN VERSUS MESSINIAN WATERS: TWO DIFFERENT CHEMICAL**

112   **SYSTEMS**

113   The salinities of modern and Messinian fluid inclusions (see GSA Data Repository)

114   are shown on Na^+ *vs* Cl^- and Ca^{2+} *vs* SO_4^{2-} plots, along with the computer-simulated

115   evaporation of seawater (Fig. 3). Salinities from modern gypsum fluid inclusions (26 weight

116   % NaCl equivalent) fall along the gypsum precipitation segment. The obtained values (Figs.

117   3A, B) are somewhat higher than the salinities of the corresponding solar saltworks brines

118   (Table 1) because (1) some water may have been lost from inclusions by evaporation, or (2)

119   the gypsum (and inclusions) formed from a more concentrated brine than that shown in Table

120   1. Nevertheless, microthermometry of modern fluid inclusions predicts that the brines from

121   which gypsum forms in marine settings are quite saline, from 11 to 27%.

122   Messinian fluid inclusions, in this study, have completely different chemical

123   compositions; their salinities range from 0.2 to 7.7% (average 1.6 weight % NaCl

124   equivalent), indicating that the brine from which gypsum formed was depleted in Na^+ and Cl^-

125   relative to seawater (Figs. 3A, B). In comparison, gypsum first precipitates during the

126   evaporation of modern seawater at a salinity of ~11%, corresponding to Tm_{ice} of $-7°$ to -8 °C

127   (Attia et al., 1995). Remarkably, no Messinian fluid inclusions have salinities high enough to

128   fall in the gypsum precipitation segment of the seawater evaporation curve (Fig. 3B). The

129   only reasonable explanation of these results is that Messinian gypsum precipitated from

130   brines with a significant proportion of non-marine waters.

131   **PALEOENVIRONMENTAL IMPLICATIONS**

132   The non-marine composition of Piedmont Messinian fluid inclusions opens new

133   questions concerning the Ca^{2+} and SO_4^{2-} sources necessary for the formation of thick gypsum

134   deposits during the Messinian salinity crisis. The commonly accepted paleohydrologic

135   models for the formation of the Primary Lower Gypsum (PLG) in the Mediterranean include

136   evaporation of brines formed by continuous inflow of seawater from the Atlantic Ocean,

137   providing the necessary ion supply, coupled with persistent reduced outflow during the

138   precessional insolation minima (Krijgsman and Meijer, 2008; Topper and Meijer, 2013). A

139   different mechanism, able to produce the lower salinity, Ca^{2+} and SO_4^{2-} enriched waters

140   found in fluid inclusions in the PLG from the Piedmont Basin (PB), involves leaching

141   ("recycling") of existing $CaSO_4$ evaporites by seawater, continental waters ("freshwater"), or

142   a combination of the two (e.g., Cendón et al., 2004; Lowenstein and Risacher, 2009). Fluid

143   inclusions composed of seawater or freshwater that have dissolved gypsum to reach

144   saturation have final ice melting temperatures of $-2°$ and ~0 °C, respectively (Attia et al.,

145   1995). Those ice melting temperatures bracket the Tm_{ice} of most of the studied samples (-1.5

146   °C $< Tm_{ice} < -0.2$ °C), which suggests that the parent waters of the PLG were mixtures of

147   seawater and continental waters that recycled pre-existing gypsum. Inflow of continental

148   freshwaters is required for all samples with fluid inclusion ice melting temperatures above -2

149   °C, the temperature of final ice melting for seawater with recycled $CaSO_4$.

150   Sulfur isotope values from Messinian sulfates in the PB ($\delta^{34}S \sim 22‰$; Fontes et al.,

151   1987) are diagnostic of Messinian seawater and/or recycled Messinian gypsum sources of

152   sulfate; a few values ($\delta^{34}S \sim 10‰$) may indicate precipitation from continental freshwater

153   enriched in sulfate dissolved from Alpine Permian and Triassic evaporites (Fontes et al.,

154   1987). Strontium isotope values from Piedmont gypsum ($0.70895 < {}^{87}Sr/{}^{86}Sr < 0.70899$;

155   Bernardi, personal commun.) also suggest Messinian seawater or recycled Messinian gypsum

156   Sr sources (Flecker et al., 2002; Lu and Meyers, 2003; Lugli et al., 2010). Sulfur and

157   strontium isotopes confirm seawater inflow to the PB. Contemporaneous low salinity

158   freshwater inflow contributed water to the PB but did little to influence the Messinian

159   seawater signal demonstrated by S and Sr isotopes. Mixed seawater-freshwater inflow is also

160   supported by the marine and freshwater diatoms found in the PLG.

161   The apparent paradox of Messinian gypsum formed from non-marine waters can be

162   explained by considering short-term changes of the hydrological budget of marginal basins

163   (Manzi et al., 2012). Deposition of the PLG deposits is here interpreted as follows: 1) during

164   the dry season evaporative concentration caused the formation of brines and, eventually, the

165   precipitation of gypsum. In the deepest anoxic settings saturation was not reached and no

166   gypsum was deposited (de Lange and Krijgsman, 2010); 2) during the wet season,

167   undersaturated continental waters (e.g., fluvial floods) partially or totally dissolved

168   previously formed marine gypsum at the shallow water margins of the PB, producing waters

169   enriched in Ca^{2+} and SO_4^{2-} but impoverished in Na^+ and Cl^-. Those "mixed" brines were the

170   parent waters for gypsum precipitation by evaporative concentration during the transition to

171   the next dry cycle.

172   This model for the PB needs to be tested for other Mediterranean PLG deposits, in

173   order to solve the conundrum of similar evaporite facies deposited under different

174   hydrological conditions. The PLG deposits show a surprisingly similar facies association and

175   stacking pattern across the whole Mediterranean (Lugli et al., 2010), suggesting shared

176   depositional conditions. On the other hand the stable isotope datasets (e.g., Pierre and Fontes,

177   1978) point to a system of sub-basins characterized by different marine and continental water

178   inflows because of their paleogeographic position or local climate. Future studies will also

179   focus on the gypsum organic content and the possible role of microbially-mediated redox

180   reactions in sulfate enrichment and gypsum precipitation.

181   **CONCLUSIONS**

182   The results of the first detailed analysis of fluid inclusion salinities in Messinian

183   gypsum crystals provide new constraints for hydrologic models explaining widespread

184   gypsum precipitation in marginal basins during the first stage of the Messinian salinity crisis.

185   This study demonstrates that at the northernmost offshoot of the Mediterranean Basin,

186   gypsum did not form just from pristine evaporated seawater but rather from a mix of seawater

187   and Ca^{2+} and SO_4^{2-} enriched non-marine waters probably derived from partial dissolution and

188   recycling of coeval marginal marine deposits. Complex recycling processes should also be

189   taken in account for explaining the genesis of other similar Messinian gypsum deposits across

190   the Mediterranean Basin.

191   **ACKNOWLEDGMENTS**

197   sample their quarries and Saline Conti Vecchi for the water and gypsum sampling at their

198   saltworks.

199   **REFERENCES CITED**

200   Attia, O.E., Lowenstein, T.K., and Wali, A.M.A., 1995, Middle Miocene gypsum, Gulf of

201   Suez: Marine or nonmarine?: Journal of Sedimentary Research, v. 65, p. 614–626.

202   Brennan, S.T., Lowenstein, T.K., and Horita, J., 2004, Seawater chemistry and the advent of

203   biocalcification: Geology, v. 32, p. 473–476, doi:10.1130/G20251.1.

204   Cendón, D.I., Peryt, T.M., Ayora, C., Pueyo, J.J., and Taberner, C., 2004, The importance of

205   recycling processes in the Middle Miocene Badenian evaporite basin (Carpathian

206   foredeep): Palaeoenvironmental implications: Palaeogeography, Palaeoclimatology,

207   Palaeoecology, v. 212, p. 141–158, doi:10.1016/j.palaeo.2004.05.021.

208   CIESM, 2008. The Messinian Salinity Crisis from mega-deposits to microbiology—A

209   consensus report, *in* Briand, F., ed., CIESM Workshop Monographs 33, Monaco, 168 p.

210   Davis, D.W., Lowenstein, T.K., and Spencer, R.J., 1990, Melting behavior of fluid inclusions

211   in laboratory-grown halite crystals in the systems $NaCl-H_2O$, $NaCl-KCl-H_2O$, NaCl-

212         $MgCl_2-H_2O$, and $NaCl-CaCl_2-H_2O$: Geochimica et Cosmochimica Acta, v. 54, p. 591–

213   601, doi:10.1016/0016-7037(90)90355-O.

214   de Lange, G.J., and Krijgsman, W., 2010, Messinian salinity crisis: A novel unifying shallow

215   gypsum/deep dolomite formation mechanism: Marine Geology, v. 275, p. 273–277,

216   doi:10.1016/j.margeo.2010.05.003.

217   Dela Pierre, F., Festa, A., and Irace, A., 2007, Interaction of tectonic, sedimentary, and

218   diapiric processes in the origin of chaotic sediments: An example from the Messinian of

219   Torino Hill (Tertiary Piedmont Basin, northwestern Italy): Geological Society of

220   America Bulletin, v. 119, p. 1107–1119, doi:10.1130/B26072.1.

221 Dela Pierre, F., Bernardi, E., Cavagna, S., Clari, P., Gennari, R., Irace, A., Lozar, F., Lugli,

222   S., Manzi, V., Natalicchio, M., Roveri, M., and Violanti, D., 2011, The record of the

223   Messinian salinity crisis in the Tertiary Piedmont Basin (NW Italy): The Alba section

224   revisited: Palaeogeography, Palaeoclimatology, Palaeoecology, v. 310, p. 238–255,

225   doi:10.1016/j.palaeo.2011.07.017.

226 Flecker, R., De Villiers, S., and Ellam, R., 2002, Modelling the effect of evaporation on the

227   salinity–87Sr/86Sr relationship in modern and ancient marginal-marine systems: the

228   Mediterranean Messinian Salinity Crisis: Earth and Planetary Science Letters, v. 203,

229   p. 221–233, doi:10.1016/S0012-821X(02)00848-8.

230 Fontes, J.C., Filly, A., and Gaudant, J., 1987, Conditions de depot du Messinien évaporitique

231   des environs d'Alba (Piémont): Arguments paléontologiques et isotopiques: Bollettino

232   della Società Paleontologica Italiana, v. 26, p. 199–210.

233 Horita, J., Zimmermann, H., and Holland, H.D., 2002, Chemical evolution of seawater during

234   the Phanerozoic: Implications from the record of marine evaporites: Geochimica et

235   Cosmochimica Acta, v. 66, p. 3733–3756, doi:10.1016/S0016-7037(01)00884-5.

236 Krijgsman, W., and Meijer, P., 2008, Depositional environments of the Mediterranean

237   "Lower Evaporites" of the Messinian salinity crisis: Constraints from quantitative

238   analyses: Marine Geology, v. 253, p. 73–81, doi:10.1016/j.margeo.2008.04.010.

239 Krijgsman, W., Hilgen, F.J., Raf, I., Sierro, F.J., and Wilson, D.S., 1999, Chronology, causes

240   and progression of the Messinian salinity crisis: Nature, v. 400, p. 652–655,

241   doi:10.1038/23231.

242 Longinelli, A., 1979, Isotope geochemistry of some Messinian evaporites;

243   paleoenvironmental implications: Palaeogeography, Palaeoclimatology, Palaeoecology,

244   v. 29, p. 95–123, doi:10.1016/0031-0182(79)90076-2.

245 Lowenstein, T.K., and Risacher, F., 2009, Closed basin brine evolution and the influence of

246   Ca–Cl inflow waters: Death Valley and Bristol Dry Lake California, Qaidam Basin,

247   China, and Salar de Atacama, Chile: Aquatic Geochemistry, v. 15, p. 71–94,

248   doi:10.1007/s10498-008-9046-z.

249 Lowenstein, T.K., Timofeeff, M.N., Brennan, S.T., Hardie, L.A., and Demicco, R.V, 2001,

250   Oscillations in Phanerozoic seawater chemistry: evidence from fluid inclusions: Science,

251   v. 294, 5544, p. 1086–1088, doi:10.1126/science.1064280.

252 Lowenstein, T.K., Hardie, L.A., Timofeeff, M.N., and Demicco, R.V., 2003, Secular

253   variation in seawater chemistry and the origin of calcium chloride basinal brines:

254   Geology, v. 31, p. 857, doi:10.1130/G19728R.1.

255 Lu, F.H., and Meyers, W.J., 2003, Sr, S, and O_{SO4} isotopes and the depositional environments

256   of the upper Miocene evaporites, Spain: Journal of Sedimentary Research, v. 73, p. 444–

257   450, doi:10.1306/093002730444.

258 Lugli, S., Manzi, V., Roveri, M., and Schreiber, B.C., 2010, The Primary Lower Gypsum in

259   the Mediterranean: A new facies interpretation for the first stage of the Messinian

260   salinity crisis: Palaeogeography, Palaeoclimatology, Palaeoecology, v. 297, p. 83–99,

261   doi:10.1016/j.palaeo.2010.07.017.

262 Manzi, V., Gennari, R., Lugli, S., Roveri, M., Scafetta, N., and Schreiber, B.C., 2012, High-

263   frequency cyclicity in the Mediterranean Messinian evaporites: Evidence for solar-lunar

264   climate forcing: Journal of Sedimentary Research, v. 82, p. 991–1005,

265   doi:10.2110/jsr.2012.81.

266 Manzi, V., Gennari, R., Hilgen, F., Krijgsman, W., Lugli, S., Roveri, M., and Sierro, F.J.,

267   2013, Age refinement of the Messinian salinity crisis onset in the Mediterranean: Terra

268   Nova, v. 25, p. 315–322, doi:10.1111/ter.12038.

269   Natalicchio, M., Dela Pierre, F., Clari, P., Birgel, D., Cavagna, S., Martire, L., and

270   Peckmann, J., 2013, Hydrocarbon seepage during the Messinian salinity crisis in the

271   Tertiary Piedmont Basin (NW Italy): Palaeogeography, Palaeoclimatology,

272   Palaeoecology, v. 390, p. 68–80, doi:10.1016/j.palaeo.2012.11.015.

273   Panieri, G., Lugli, S., Manzi, V., Roveri, M., Schreiber, B.C., and Palinska, K.A, 2010,

274   Ribosomal RNA gene fragments from fossilized cyanobacteria identified in primary

275   gypsum from the late Miocene, Italy: Geobiology, v. 8, p. 101–111, doi:10.1111/j.1472-

276   4669.2009.00230.x.

277   Pierre, C., and Fontes, J.C., 1978, Isotope composition of Messinian sediments from the

278   Mediterranean Sea as indicators of paleoenvironments and diagenesis, *in*: Hsü, K.J., and

279   Montadert, L., eds Initial Reports of the Deep Sea Drilling Project, Leg XLIIA,

280   Washington, US Government Printing Office, v. 42A, p. 635–650.

281   Roveri, M., Lugli, S., Manzi, V., and Schreiber, B.C., 2008, The Messinian Sicilian

282   stratigraphy revisited: new insights for the Messinian Salinity Crisis: Terra Nova, v. 20,

283   p. 483–488.

284   Sabouraud-Rosset, C., 1976, Solid and liquid inclusions in gypsum [unpublished These

285   d'Etat]: Paris, Université Paris Sud, Centre d'Orsay, 173 p.

286   Topper, R.P.M., and Meijer, P.T., 2013, A modeling perspective on spatial and temporal

287   variations in Messinian evaporite deposits: Marine Geology, v. 336, p. 44–60,

288   doi:10.1016/j.margeo.2012.11.009.

289   **FIGURE CAPTIONS**

290   Figure 1. A: Distribution of the Messinian evaporites (gypsum and halite) in the

291   Mediterranean Basin (after Lugli et al., 2010 and Manzi et al., 2012). PB: Piedmont Basin;

292   CV: Conti Vecchi saltworks. B: Geological sketch of the studied area showing the

293   distribution of the Messinian sulfates and of the sampled sections (M: Moncucco; B:

294   Banengo).

295   Figure 2. Messinian and modern gypsum. A: Panoramic view of the Moncucco quarry: three

296   Primary Lower Gypsum couplets, composed of mud (M; dashed lines) and gypsum (G), are

297   visible; arrows indicates the gypsum growth direction. B: Twinned Messinian selenite crystal;

298   TI: turbid interval; LI: limpid interval. C: Modern gypsum dome, Conti Vecchi saltworks;

299   arrows point to dissolution surfaces among cm-sized crystal palisades. D,E,F:

300   Photomicrographs of primary (D, E) and secondary (F) fluid inclusions in Messinian crystals

301   (transmitted light); E shows a primary fluid inclusion near the Tm_{ice}, with ice, liquid, and

302   vapor. G,H: Photomicrographs of primary fluid inclusions in modern gypsum (transmitted

303   light); H shows melting of hydrohalite microcrystals in the presence of liquid and vapor.

304   Figure 3. Na^+ *vs* Cl^- (A) and Ca^{2+} *vs* SO_4^{2-} (B) diagrams showing the curve tracking computer

305   simulation of the evaporation of modern seawater (see details in GSA Data Repository) and

306   the composition of the Conti Vecchi brine (circle). Messinian (bars) and modern (vertical

307   dashed line) fluid inclusions salinities are reported as weight % NaCl equivalent (bottom

308   scale). Vertical axis on the left refers to the number of Messinian fluid inclusions. The

309   salinity of modern seawater is also reported for comparison (vertical line). The minerals

310   predicted to precipitate during progressive evaporation of seawater are shown as horizontal

311   bars at the bottom.

312   [1]GSA Data Repository item 2014XXX sampling, methodology and Messinian fluid inclusion

313   data (Table DR1, Figure DR1) are available online at www.geosociety.org/pubs/ft2014.htm,

314   or on request from editing@geosociety.org or Documents Secretary, GSA, P.O. Box 9140,

315   Boulder, CO 80301, USA.

TABLE 1. CONTI VECCHI BRINE COMPOSITION
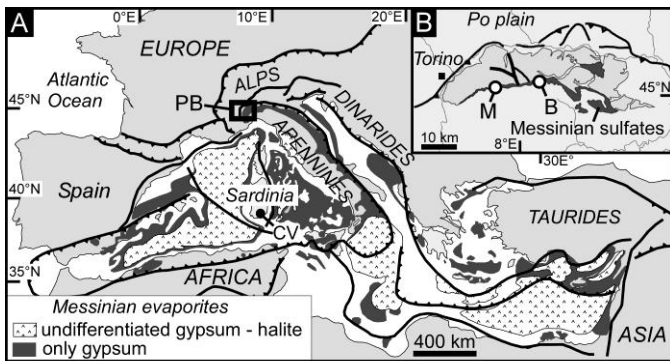
Sample name	Cl (*)	SO$_4$ (*)	Br (*)	Ca (*)	K (*)	Mg (*)	Na (*)	Sr (*)	Conductivity (mS/cm)	Salinity (PSU)	Density (g/mL)
CV1	4070	158	5.8	25	105	522	3980	0.5	211	212	1.15

Note: (*) Units are in millimols solute per kg H_2O

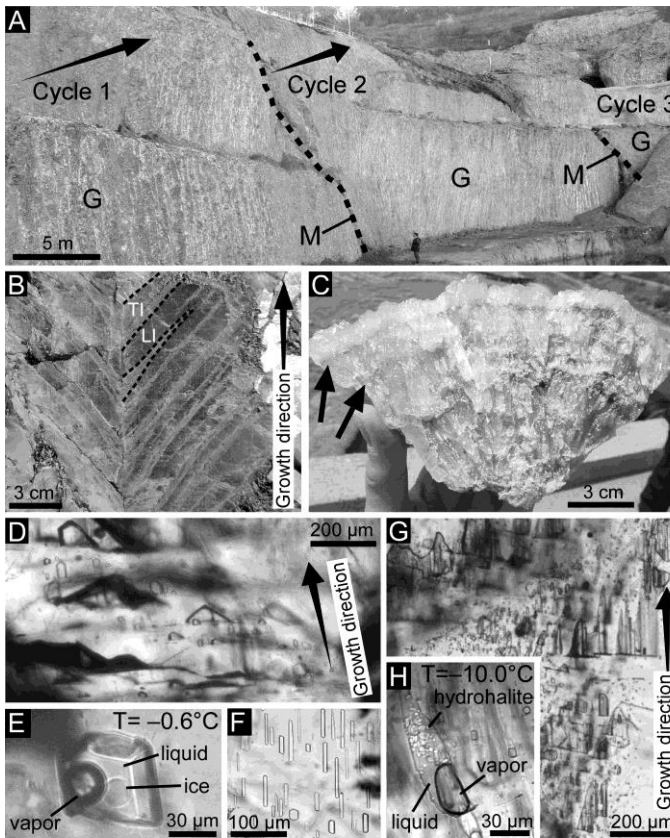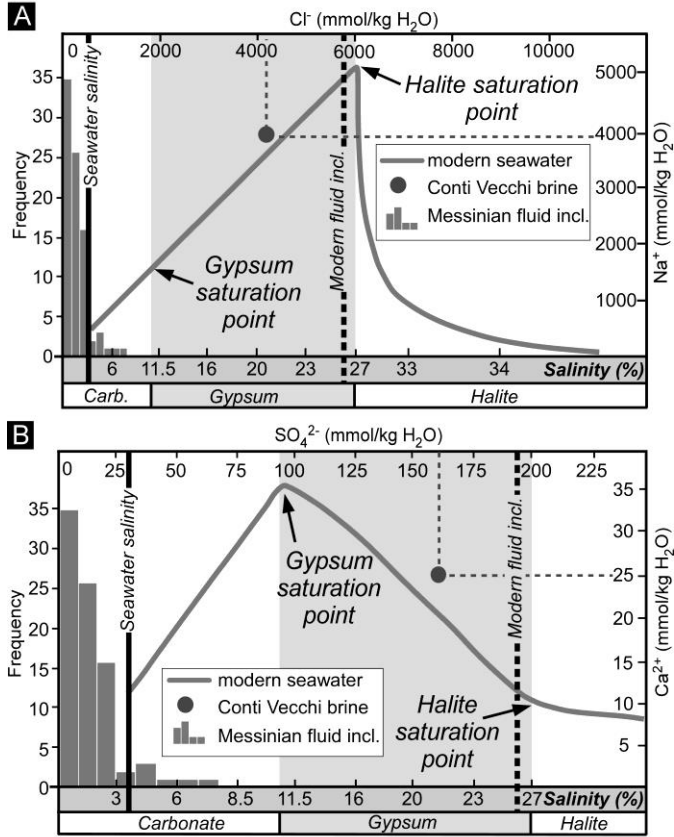316   FIGURES

317

318   Natalicchio et al. Fig. 1 (JPG)

319

320   Natalicchio et al. Fig. 2 (JPG)

321

322   Natalicchio et al. Fig. 3 (JPG)

323